




Article

Highly Selective Removal of Cationic Dyes from Wastewater by MgO Nanorods

Monira Galal Ghoniem¹, Fatima Adam Mohamed Ali^{1,*}, Babiker Yagoub Abdulkhair¹ ,
Mohamed Rahmt Allah Elamin¹, Arwa Mofareh Alqahtani¹, Seyfeddine Rahali^{2,*} , and Mohamed Ali Ben Aissa^{2,*} 

¹ Department of Chemistry, College of Science, Imam Mohammad Ibn Saud Islamic University (IMSIU), Riyadh 11432, Saudi Arabia; mgghoniem@imamu.edu.sa (M.G.G.); babiker35.by@gmail.com (B.Y.A.); mohamedrahmt99@gmail.com (M.R.A.E.); amalqhtani@imamu.edu.sa (A.M.A.)

² Department of Chemistry, College of Science and Arts, Qassim University, Ar Rass, Saudi Arabia

* Correspondence: Famohamedali@imamu.edu.sa (F.A.M.A.); saif.rahali@gmail.com (S.R.); dalibenissa@gmail.com (M.A.B.A.)

Abstract: The organic synthetic dyes employed in industries are carcinogenic and harmful. Dyes must be removed from wastewater to limit or eliminate their presence before dumping into the natural environment. The current study aims to investigate the use of MgO nanoparticles to eliminate basic fuchsine (BF), as a model cationic dye pollutant, from wastewater. The MgO nanorods were synthesized through a coprecipitation method. The obtained nanocomposite was characterized using various techniques such as X-ray diffraction (XRD), field emission scanning electron microscopy (FE-SEM), Brunauer–Emmett–Teller (BET), and FTIR spectroscopy. It was found that the variation of dye concentration and pH influenced the removal of BF by MgO. The adsorption capacity of 493.90 mg/g is achieved under optimum operating conditions (pH = 11, contact time = 236 min, and initial BF concentration = 200 ppm). Pseudo-second-order adsorption kinetics and Freundlich isotherm models best fitted BF sorption onto MgO nanorods. The BF sorption mechanism is associated with the electrostatic attractions and hydrogen bond between the O–H group of MgO and the NH₂ groups of BF, as indicated by the pH, isotherms, and FTIR studies. The reusability study indicates that MgO was effectively used to eliminate BF in at least four continuous cycles. The investigation of MgO with different dyes suggests the high adsorption selectivity of BF, crystal violet (CV), and malachite green (MG) dyes compared with methyl orange (MO) dye. Overall, MgO nanorods can act as a potential and promising adsorbent for the efficient and rapid removal of cationic dyes (CV, MG, and BF) from wastewater.

Keywords: MgO nanomaterials; basic fuchsine elimination; pH influence; kinetics experiment



Citation: Ghoniem, M.G.; Ali, F.A.M.; Abdulkhair, B.Y.; Elamin, M.R.A.; Alqahtani, A.M.; Rahali, S.; Ben Aissa, M.A. Highly Selective Removal of Cationic Dyes from Wastewater by MgO Nanorods. *Nanomaterials* **2022**, *12*, 1023. <https://doi.org/10.3390/nano12061023>

Academic Editors: Yuxin Zhang and Shude Liu

Received: 16 February 2022

Accepted: 14 March 2022

Published: 21 March 2022

Publisher's Note: MDPI stays neutral with regard to jurisdictional claims in published maps and institutional affiliations.



Copyright: © 2022 by the authors. Licensee MDPI, Basel, Switzerland. This article is an open access article distributed under the terms and conditions of the Creative Commons Attribution (CC BY) license (<https://creativecommons.org/licenses/by/4.0/>).

1. Introduction

Organic synthetic dyes are extensively used in various industries, including in printing, textiles, paints, and pigments [1]. The discharge of dye effluents from various industries has posed a grave hazard to the marine environment and human health. Additionally, most dyes are extremely poisonous and can have mutagenic, carcinogenic, and teratogenic impacts on humans and aquatic life at extremely low concentrations [2]. Cationic dyes have been reported to be more toxic than anionic dyes, with tinctorial values of 1 mg/L [3]. Basic fuchsine (BF) is a cationic dye utilized in diverse fields, including biological stains and leather, paper, and cotton coloring agents [4,5]. Additionally, it is referred to as basic violet or rosaniline chloride [6]. It is a member of a triphenylmethane dye class with the chemical formula C₂₀H₂₀ClN₃ [7] and boasts an impressive planar conjugated π structure (Figure 1) [8]. Despite this, the basic fuchsine (BF) dye is combustible, anesthetic, and bacteriostatic [9,10]. It has been classified as a probable carcinogen in several nations because of its toxicity, carcinogenicity, and poor biodegradability [11,12]. As a result, much effort has been devoted to removing BF from wastewater. A variety of physical, chemical,

and biological strategies have been employed to remove dye pollutants from environmental wastewater, including biodegradation [13], chemical oxidation [14], ion exchange [15,16], membrane filtration [17], and adsorption [18–20]. Even though photocatalysis is a simple, highly efficient, and advantageous technique for removing dye contaminants [21], it has some drawbacks. It is not a cost-effective approach, photocatalysts leach into the water system, and it is ineffective in dark conditions [22]. The adsorption method is considered the most effective technology for removing dye pollutants from water due to its low cost, high efficiency, versatility, and ease of use [23]. The critical component of this approach is the development of high-performance adsorbents. Numerous studies have been conducted to explore nanomaterials as efficacious sorbents for the elimination of cationic dyes from used water [24,25]. Several nanomaterials, including $Y_2O_3@ZnO$ [18], $TiO_2/MWCNTs$ [20], and starch-capped zinc selenide [26], have been investigated as adsorbents for BF elimination from wastewater.

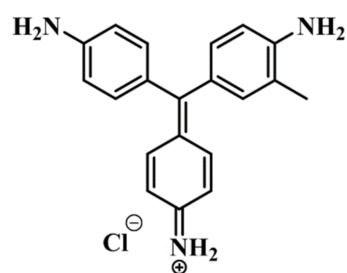


Figure 1. Chemical structure of basic fuchsine (BF).

Magnesium oxide (MgO) exhibits excellent surface characteristics at the nanoscale due to its polyhedral structure and the formation of Frenkel or Schottky defects at the edge/corner [27]. These features result in a high surface area for the nanomaterials, making them applicable for environmental remediation.

The current study aims to investigate the manufacturing of MgO nanorods and evaluate their adsorption ability to remove cationic dyes. The MgO characteristics were studied using SEM, BET, XRD, and FTIR. The effectiveness of the elimination parameters such as contact time, initial BF concentration, and pH toward the sorption capability of MgO nanorods was examined. Additionally, kinetic studies, adsorption isotherms, and reusability were also studied. The plausible mechanism of BF dye removal by MgO nanoparticles was scrutinized by FTIR and pH studies.

2. Experimental

2.1. Chemicals

Magnesium nitrate ($\geq 99.0\%$), ammonia solution (NH_4OH , 25%), basic fuchsine (BF, $\geq 85\%$), malachite green (MG, $\geq 90\%$), crystal violet (CV, $\geq 90\%$), methyl orange (MO, $\geq 85\%$), sodium hydroxide (NaOH, $\geq 99\%$), sodium chloride (NaCl, $\geq 99\%$), and hydrochloric acid (HCl, 37%) purchased from Merck Company were used without further purification. The required concentrations (25 to 300 ppm) were obtained by diluting the BF stock solution (500 ppm).

2.2. Preparation of MgO Nanorods

Magnesium oxide nanorods were synthesized in two steps: magnesium hydroxide precipitation and then calcination at $700\text{ }^\circ\text{C}$ until MgO formation. Magnesium hydroxide $Mg(OH)_2$ was obtained by adding increments of aqueous ammonia (NH_4OH) to 200 mL of magnesium nitrate solution (0.1 M) until precipitation and keeping constant stirring using a magnetic stirrer for 12 h. The precipitate was washed, dried, and calcined using a combustion furnace at $700\text{ }^\circ\text{C}$ for about 2 h [28].

2.3. Characterization of MgO Nanorods

Field emission scanning electron microscopy (FE-SEM) was used to study the morphology of the as-prepared MgO nanorods using a high-resolution JEOL JEM-6700F apparatus integrated with electron dispersive X-ray spectroscopy (EDS) for elemental chemical composition determination. X-ray diffraction (XRD) was used to determine the crystal structure and phase purity using a Rigaku Mini Flex 600 (Tokyo, Japan) diffractometer equipped with a CuK radiation source ($\lambda = 1.5417 \text{ \AA}$). The Brunauer–Emmett–Teller (BET) formula and Lippens and de Boer's t-plot approach were used to determine the surface area and porosity of MgO. The vibration modes of MgO nanorods were determined before and following BF dye adsorption using a JASCO FT-IR spectrometer.

2.4. Dye Adsorption Experiment

Batch elimination investigations were carried out by putting 10 mg of MgO nanorods in 25 mL of dye solution with varying beginning concentrations C_0 (25–300 ppm) on a magnetic stirrer for 24 h. Following each experiment, the samples were centrifuged, and the dye concentrations were concluded using a Shimadzu spectrophotometer (UV-1650 PC). The remaining dye concentration was obtained at a maximum wavelength of 545 for BF, 590 nm for CV, 579 nm for MG, and 465 nm for MO. The spectrophotometer was used to estimate the dye concentrations C_t at t time and C_e at the equilibrium. The following equation was used to determine the organic dye capacity (q_e):

$$q_e = (C_0 - C_e) \frac{V}{m} \quad (1)$$

For the kinetic study, the mass of MgO (m), the initial concentration, and the volume of BF solutions were 60 mg, 200 ppm, and 150 mL (V), respectively. At fixed intervals of time, 5 mL of the mixture was retired and centrifuged for determining the residual BF concentration [29]:

$$q_t = (C_0 - C_t) \frac{V}{m} \quad (2)$$

The BF sorption on the as-prepared MgO was investigated, the adsorption capacity (q_t) and percentage (Ads %) were calculated utilizing Equations (3) and (4), respectively.

$$q_t = \frac{(C_0 - C_t) V}{M} \quad (3)$$

$$\text{Ads \%} = \frac{(C_0 - C_t)}{C_0} \times 100 \quad (4)$$

C_0 (mg L^{-1}) and C_t (mg L^{-1}) represent initial and unadsorbed concentrations; M (kg) and V (L) represent the solution's volume and sorbent's mass. Remarkable fast uptake and high experimental q_t are the most important properties for excellent sorbents. In our case, both conditions were fulfilled as the prepared MgO possessed a practical adsorption capacity of 496 mg/g.

3. Results and Discussion

3.1. MgO Characterizations

To illustrate the structural and morphological properties of the nanomaterial as-synthesized, SEM micrographs of the obtained MgO nanomaterials are shown in Figure 2a. MgO appears to have a rod-like structure. The elemental composition and elemental mapping of the produced MgO were determined using EDS in conjunction with SEM (Figure 2b). In addition to the oxygen peak, the EDS analysis of MgO revealed the presence of a powerful and sharp magnesium peak without any impurity peak. The elemental mapping of the produced nanomaterials revealed that Mg and O were distributed uniformly within the MgO (Figure 2d,e).

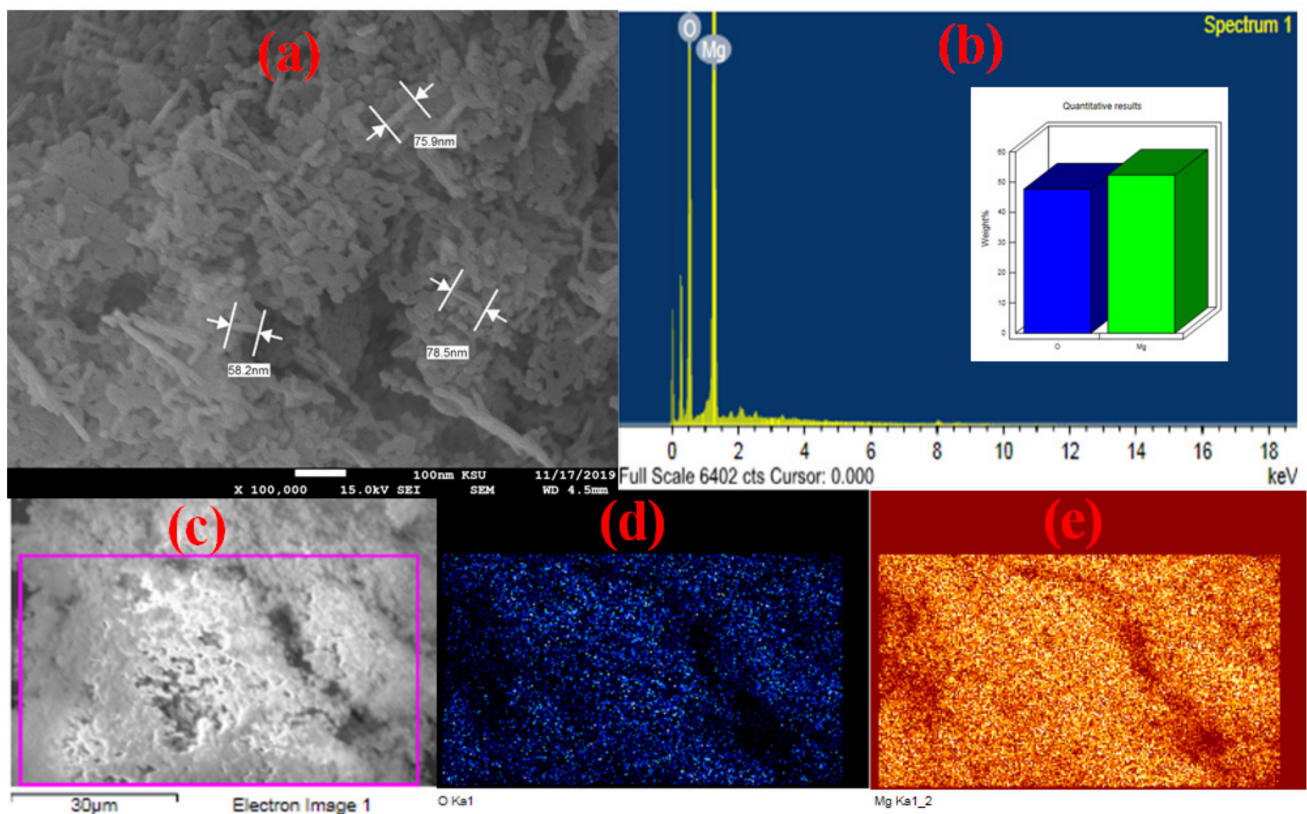


Figure 2. (a) SEM image and (b) EDX spectrum of MgO; X-ray elemental mapping of (d) Mg–K α and (e) O–K α of the SEM selected area (c).

The XRD pattern of the as-obtained MgO nanorods is illustrated in Figure 3a. The main diffraction peaks at $2\theta = 78.7, 74.8, 62.3, 43.0,$ and 37.1° could be indexed to the (222), (311), (220), (200), and (111) planes of MgO structure (JCPDS 87-0653) [30]. No impurity peaks were found, indicating that the MgO nanorods formed were pure.

Figure 3b illustrates the FTIR spectra of the as-fabricated MgO nanorods. The sharp and strong band at 3725 cm^{-1} was assigned to the $A_{2u}(\text{OH})$ lattice vibration [31]. The large band at 3438 cm^{-1} was assigned to the stretching vibration of the O–H group [32]. Bands in the range $1458\text{--}1640\text{ cm}^{-1}$ were linked to the adsorbed water molecule's –OH stretching mode. It is widely recognized that MgO can react with water to generate $\text{Mg}(\text{OH})_2$ [33]. The characteristic bond occurred at 820 cm^{-1} , confirming the existence of MgO bands [32]. The pore size distribution and N_2 adsorption–desorption isotherms of the as-obtained MgO nanoparticles are exhibited in Figure 3c,d, respectively. The results indicate that the isotherm is a type IV hysteresis buckle with H3 hysteresis buckle [34]. The MgO nanoparticles' average pore diameter and BET surface area are 1.7 nm and $12.215\text{ m}^2/\text{g}$, respectively.

3.2. Adsorption of BF

3.2.1. Influence of Dye Concentration and pH on BF Adsorption

The studies on the influence of dye concentration were performed at $\text{pH} = 7$ using varied BF concentrations (from 25 to 300 ppm). The adsorption experiments were conducted employing 10 mg of MgO nanoparticles and 25 mL of BF solution. Figure 4a shows that the adsorbed amount of BF increases from 65.45 to 738.79 mg/g when the initial BF concentration increases. When the initial BF concentration increases, the effective driving force generated overcomes any resistance of BF migration from the solution [35,36].

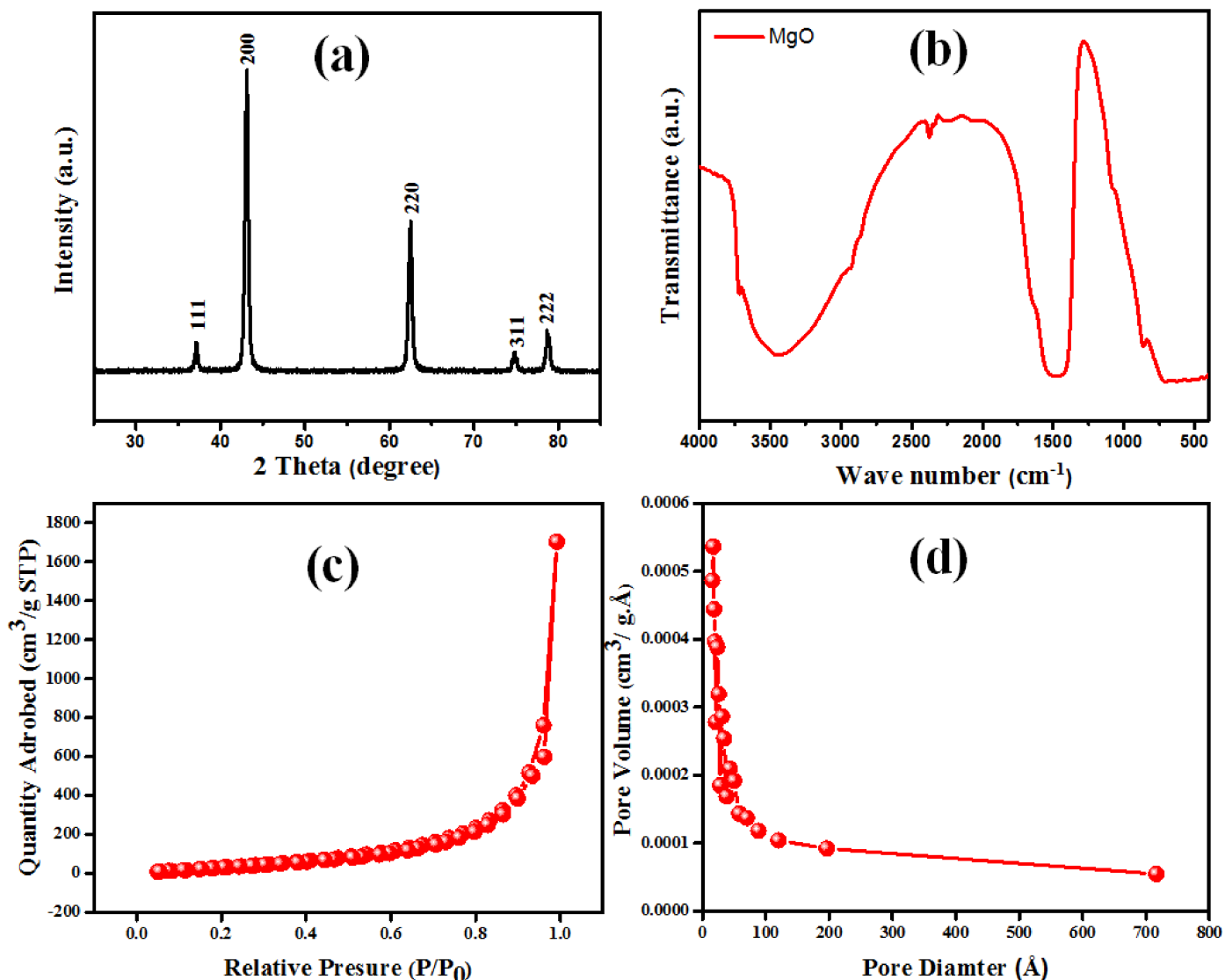


Figure 3. (a) XRD patterns, (b) FTIR spectra, (c) pore size distribution, and (d) nitrogen adsorption–desorption isotherm of MgO nanorods.

Many studies prove that the solution pH value plays a crucial role in the adsorption process by modifying the surface charge of nanomaterials [23,37]. Therefore, the surface is positively charged at pH lower than pHzpc value and negatively charged at pH greater than pHzpc value. The MgO's pHzpc was obtained using the solid addition method. [38]. Starting with a solution of KNO_3 (0.1 M), the pH of the solution was adjusted from 3 to 11 by gradually adding HCl or NaOH solutions. Then, 10 mg of adsorbent was added to 10 mL of pH-adjusted KNO_3 solution (pH_i) and stirred for one hour. After that, the final solution pH (pH_f) was measured, and the difference between the pH_f and pH_i was plotted versus the pH_i (Figure 4b). The point where $\text{pH}_f - \text{pH}_i = 0$ was designated the pHzpc equal to 9.2 for MgO (Figure 4b). To explain the effect of the solution pH value on the BF dye elimination performance, the pH experiment was carried out employing 10 mg of MgO with an initial BF concentration of 200 ppm that was regulated at 3, 5, 7, 9, and 11 pH values. The pH's effect on BF elimination performance is shown in Figure 4c. It can be remarked that low adsorption efficiency was obtained at acidic pH values, while higher elimination efficacy of BF was attained at basic pH values. The low adsorption efficiency obtained at lower pH values is due to electrostatic repulsion between the MgO sorbent and the BF dye [39]. The electrostatic attraction between MgO and BF molecules improves the dye adsorption at basic pH [40].

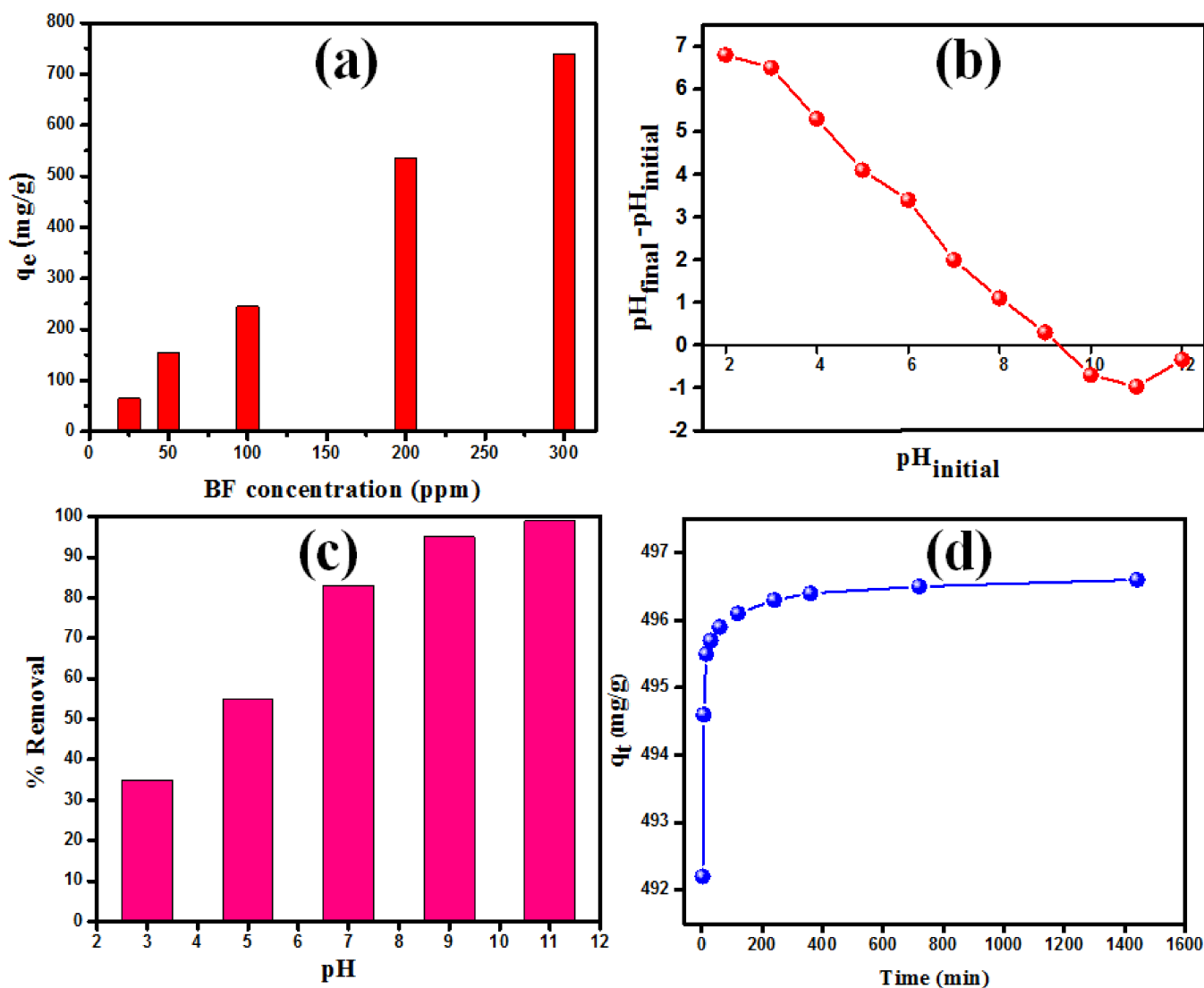


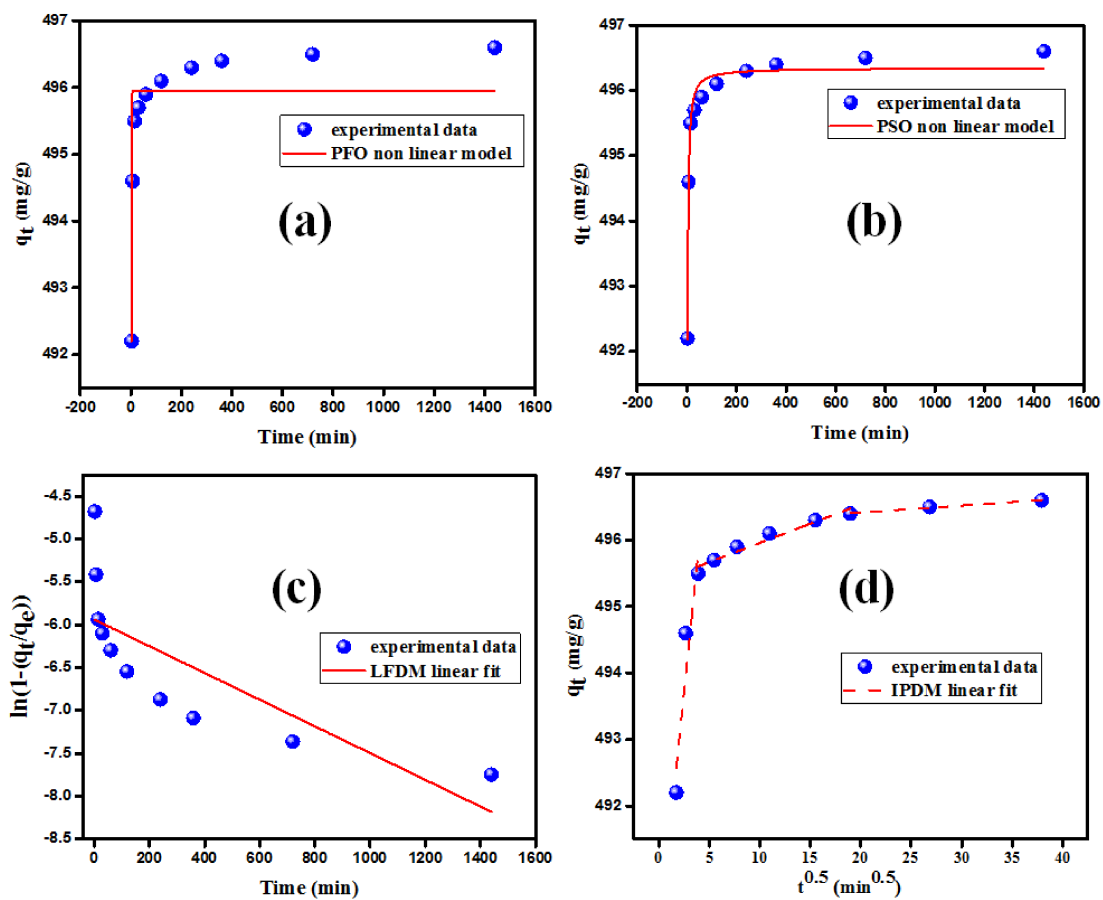
Figure 4. (a) Effect of initial BF dye concentration on the adsorption on MgO at pH = 7, (b) plot for the determination of pHZPC of MgO, (c) the influence of pH on % elimination of BF with an initial concentration of 200 ppm, and (d) equilibrium time study with a BF starting concentration of 150 ppm.

3.2.2. Kinetics of BF Adsorption on MgO Nanorods

At room temperature, the effect of agitation time on the adsorption of BF molecules onto MgO nanorods was investigated by altering the agitation period between 5 and 1440 min with a BF starting concentration of 150 ppm (see Figure 4d). The rate of BF elimination increases steadily as the contact time increases and achieves equilibrium within 236 min. At the start of the procedure, the adsorption rate was extremely rapid due to the accessibility of a high number of active sites on the surface of MgO nanorods. The equilibrium concentration of the remaining active sites is lowered, and the sorption rate becomes extremely low. As a result, the elimination of BF molecules is unaffected. The nonlinear formulas of the adsorption kinetic were utilized to avoid spurious findings of the linearized equations [41,42]. Hence, the original equations of pseudo-first-order (PFO) and pseudo-second-order (PSO) (Table 1) were employed [43–45]. k_1 (min^{-1}) and k_2 ($\text{g mg}^{-1} \text{min}^{-1}$) presented the rate constants for PFO and PSO, respectively. The k_1 and k_2 values were extracted from the obtained slope values of the PFO and PSO plots (Figure 5) [46].

Table 1. The kinetic parameters for BF sorption on MgO nanoparticles.

Kinetics Model	Kinetic Equation	Parameter	Value
Pseudo-first-order [43]	$q_t = q_e(1 - \exp^{-K_1 t})$	q_e	495.9
		K_1	1.62
		R^2	0.80
Pseudo-second-order [47]	$q_t = \frac{k_2 q_e^2 t}{1 + k_2 q_e t}$	q_e (exp)	496.81
		q_e (cal)	496.34
		K_2	0.0715
		R^2	0.98
Liquid film diffusion [45]	$\ln\left(1 - \left(\frac{q_t}{q_e}\right)\right) = -K_{LF} t$	K_{LF} (min^{-1})	5936
		R^2	0.60
		K_{dif1} ($\text{mg/g min}^{0.5}$)	1.496
Intra-particle diffusion [48]	$q_t = k_{dif} t^{1/2} + C$	C_1 (mg/g)	489.9
		R^2	0.95
		K_{dif1} ($\text{mg/g min}^{0.5}$)	0.057
		C_2 (mg/g)	495.4
		R^2	0.94
		K_{dif3} ($\text{mg/g min}^{0.5}$)	0.010
		C_3 (mg/g)	496.2
R^2	0.99		

**Figure 5.** (a,b) Nonlinear pseudo-first-order and pseudo-second-order kinetic plots; (c,d) the liquid film diffusion model and intraparticle diffusion model plots.

The best-fitted kinetic model was selected according to the correlation coefficient values (R^2) and the q_t values calculated from the regression [41]. The obtained results indicated that BF adsorption on MgO nanoparticles followed the PSO with an estimated q_t value similar to the experimental one (Table 1 and Figure 5).

The preliminary data analysis established that the PSO kinetic model is suitable for modeling the adsorption of BF onto MgO nanorods. This includes the entire adsorption process involving liquid film diffusion (LFDM), adsorption on the adsorbent surface, and intraparticle diffusion (IPDM) [49,50]. Due to the accelerated rate, the general adsorption response cannot be regarded as a controlling step in the adsorption process. Thus, the rate of adsorption was mostly determined by slower stages such as LFDM and IPDM, either alone or together. The equations of intraparticle (IPDM) [48] and liquid-film diffusion models (LFDM) [51] are presented in Table 1. K_{LF} (min^{-1}) and the K_{dif} ($\text{mg/g min}^{-0.5}$) are LFDM and IPDM factors. C_i (mg/g) is a factor that represents a boundary layer thickness. The linear regression plots for LFDM and IPDM are illustrated in Figure 5, and the results extracted from the graphs are displayed in Table 1. The BF sorption on MgO appeared to be controlled by the IPDM, as determined by the R^2 values, and three linear segments can be seen when piecewise linear regression is used. In addition, the IPDM fitting curve did not pass through the origin point, implying that the primary rate-controlling mechanism is intraparticle diffusion [50].

3.2.3. Adsorption Equilibrium

One of the most significant characteristics of adsorbents is the uptake capacity. Here, this is the maximum quantity (q_{\max}) of BF that MgO can remove. To calculate the uptake capacity of MgO nanoparticles, the adsorption results were adopted for the most used adsorption isotherms: Temkin, Dubinin–Radushkevich, Freundlich, and Langmuir. The formulas of the employed isotherm models are provided in Table 2.

Table 2. Different isotherm constants for the adsorption of BF dyes onto MgO nanorods.

Model	Equation	Parameter	Value
Langmuir [52]	$\frac{C_e}{q_e} = \frac{1}{q_m K_L} + \frac{C_e}{q_m}$	q_m (mg/g)	493.90
		K_L (mg/g)	0.04
		R_L (L/mg)	0.17
		R^2	0.985
Freundlich [53]	$\ln q_e = \ln K_F + \frac{1}{n} \ln C_e$	n	2.07
		K_F (L/mg)	176.21
		R^2	0.999
Dubinin–Radushkevich [54]	$\ln q_e = \ln q_m - K\epsilon^2$	q_m (mg/g)	504.70
		$K \times 10^{-9}$ (mol/Kj) ²	2.04
		E (Kj/mol)	6.38
		R^2	0.859
Temkin [55]	$q_e = \frac{RT}{b} \ln K_T + \frac{RT}{b} \ln C_e$	b (J/mol)	0.10
		K_T (L/mg)	2.63
		R^2	0.921

The linear isotherm graphs for BF adsorption on MgO are shown in Figure 6, and the characteristics of the adsorption isotherms are listed in Table 2. As demonstrated in the obtained results (Table 2), the Freundlich model for BF adsorption provides the best match with the greatest regression coefficient ($R^2 = 0.9957$). The great value of the exponent $n = 2.07$, in the gamut 2–10, indicates superior adsorption properties [56]. In the Dubinin–Radushkevich isothermal model, the E value ($(2K)^{0.5}$) indicates whether the adsorption

process is mainly chemical or physical [57]. The mean energy value (E) was calculated as 6.38 kJ/mol. The obtained energy value is less than 8 kJ/mol, confirming that the BF adsorption on MgO is a physisorption process [58,59].

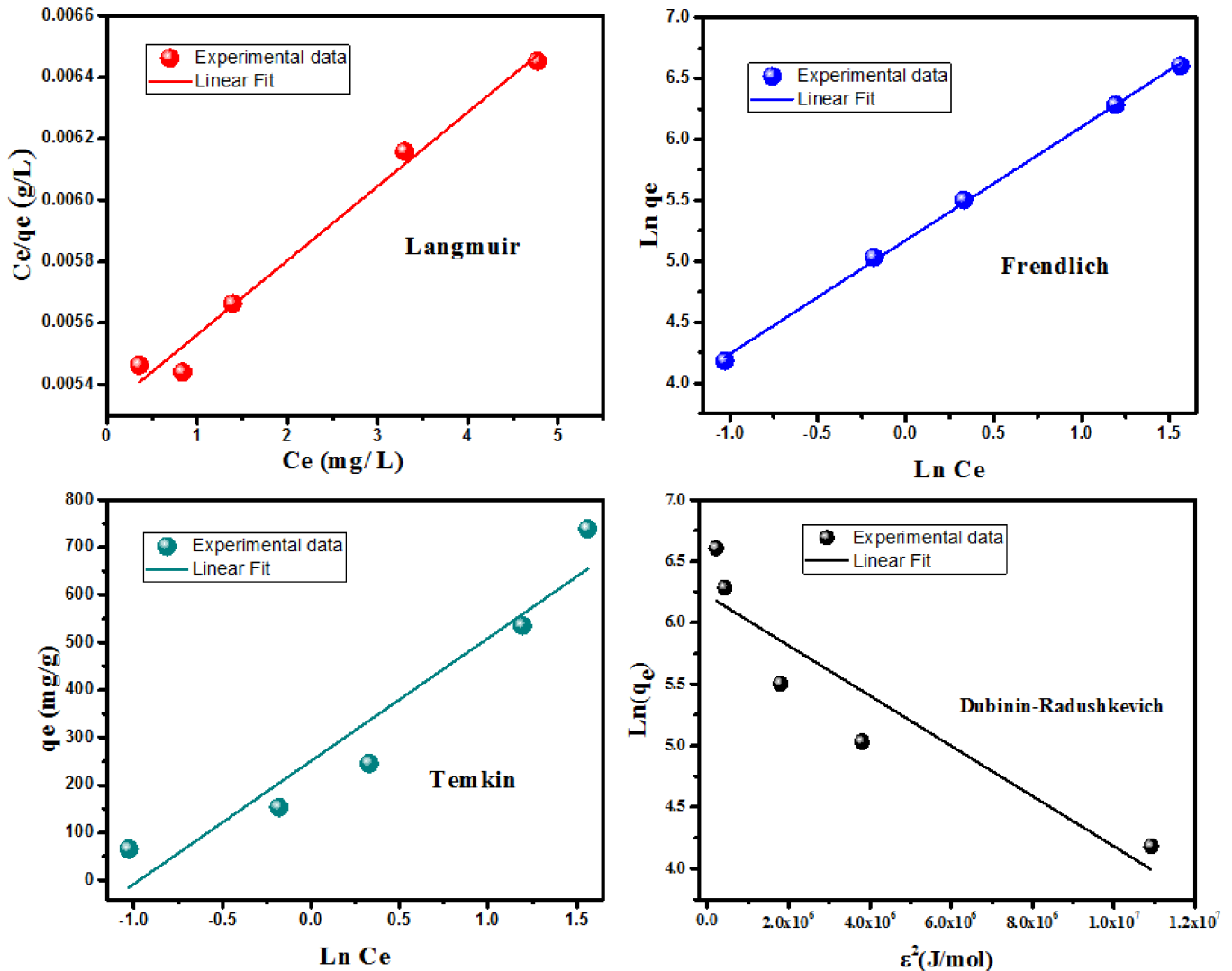


Figure 6. Adsorption of BF equilibrium models.

MgO's adsorption capacity for BF is 493.9 mg/g, according to the Langmuir isotherm model, as shown in Table 2. It is advantageous to compare the MgO adsorption capacity with several BF dye adsorbents. Table 3 reveals the various adsorption capacities of sorbents for BF removal when compared to MgO nanorods. It is noteworthy that the MgO has a higher adsorption capacity than previously reported sorbents. Indeed, under the same pH condition (pH = 12), Tabrez A. Khan et al. studied the removal of basic dyes from aqueous solution by adsorption onto binary iron–manganese oxide coated kaolinite [60]. They found that the Fe-MgO/kaolinite adsorption capacity is 10.36 mg/g, which is very low compared to that found in our study. Likewise, Bouchra Ba Mohammed et al. successfully synthesized the Fe-ZSM-5 zeolite for BF dye adsorption from aqueous solutions [61]. The maximum uptake capacity was found to be 251.87 mg/g, which is lower than that of MgO. This finding established the efficacy of MgO nanorods as a good BF adsorbent.

Table 3. Comparison of the adsorption capabilities of MgO nanorods with various adsorbents.

Adsorbent	q_e (mg/g)	pH	References
Fe-MgO/kaolinite	10.36	10–12	[60]
Fe-ZSM-5 zeolite	251.87	5.0	[61]
Al/MCM-41	54.44	5	[62]
H ₂ Ti ₃ O ₇ titanate nanotubes	183.20	2.4	[63]
ESM	47.85	6	[36]
Starch-capped zinc selenide	222.72	7.0	[26]
Modified activated carbons	238.10	7–8	[11]
Loess clay (LC)	47.49	2–5.9	[64]
MgO	493.90	12	Current work

3.3. Adsorption Mechanism

FTIR study was employed to explain BF dyes' selectivity and adsorption mechanism onto MgO nanorods. FTIR measurements were accomplished for the obtained MgO nanoparticles, Bf dye, and MgO nanoparticles after adsorption. Figure 7a presents the FTIR spectra of BF, MgO, and BF@MgO. The BF spectrum exhibits several distinct bands, including NH₂ bending (3314 and 3175 cm⁻¹), C=N stretching (1638 and 1325 cm⁻¹), and aryl CH wagging (907–831 cm⁻¹). The MgO spectrum exhibits the absorption band at 3461 cm⁻¹ attributed to the O–H stretching vibration group that demonstrates the existence of hydroxyl groups in the MgO nanoparticles. After adsorption, the O–H group of MgO interacts with the lone-pair electrons of NH₂ groups of BF via hydrogen bonds, which is confirmed by the slight shifting of the O–H stretching vibration band to 3384 cm⁻¹. The adsorption effectiveness at lower pH levels, despite the electrostatic attraction between the MgO sorbent and the BF dye, demonstrates the presence of hydrogen bonding between the BF and MgO nanoparticles. In addition, the MgO@BF spectrum exhibits the presence of the characteristic BF in shifted position relative to the free molecules, showing the presence of MgO and BF interactions. In that order, the new band at 1671 cm⁻¹ in the MgO@BF spectrum indicated the formation of ionic interactions between the BF molecules and the negative-charged MgO surface [65]. Following the pH, the study implies that the electrostatic attraction controls the BF sorption mechanism onto the MgO sorbent. The recommended BF sorption mechanism onto the MgO involves electrostatic attractions and hydrogen bonds. The recommended adsorption mechanism of the BF onto MgO nanorods is presented in Figure 7b.

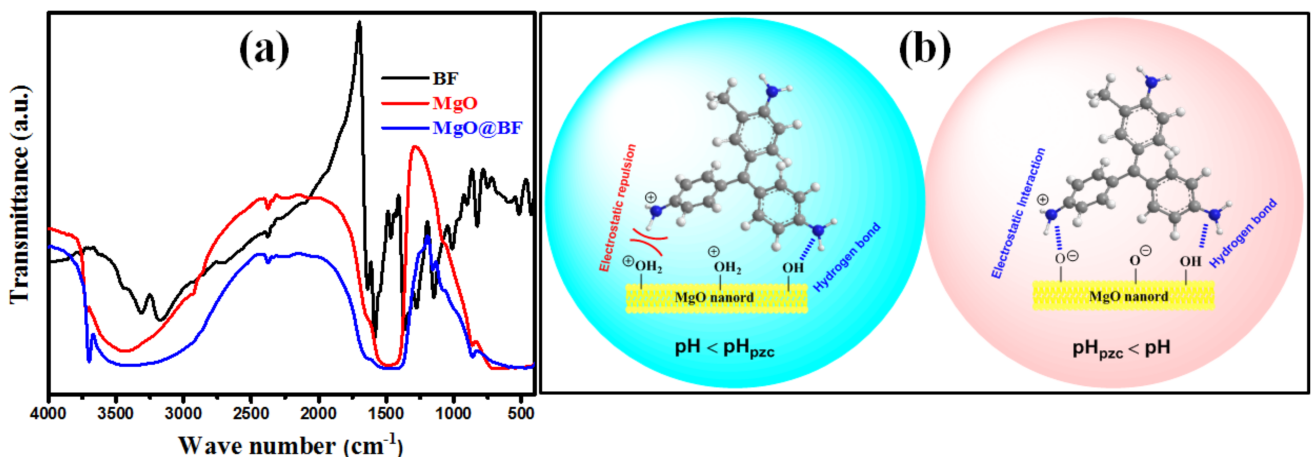


Figure 7. (a) FTIR spectra of MgO, BF, and MgO@BF and (b) the proposed adsorption mechanism of BF onto MgO nanorods.

3.4. Reusability and Selectivity Study

The reusability and the regeneration of MgO sorbent were examined by BF elimination from the surface of the nanomaterial. After the adsorption experiment, the dye desorption from the MgO was conducted by heating in an oven at 500 °C for 60 min. After that, the recuperated MgO was reused for the BF elimination. The reusability results indicate that MgO was effectively used to eliminate BF in at least four continuous cycles. (Figure 8a).

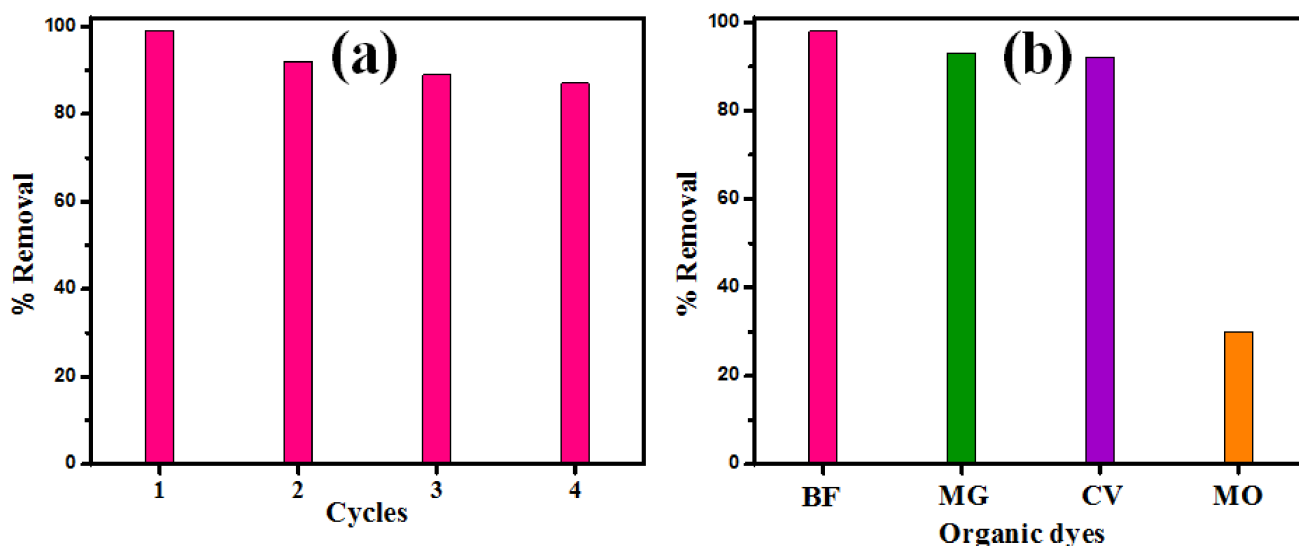


Figure 8. (a) Reusability efficiency of MgO NPs and (b) the elimination rate of different dyes by MgO adsorbent.

The high adsorption capability of MgO nanorods towards BF dye has also been examined compared to other organic dyes (BF, CV, MG, and MO). The selectivity study of MgO nanoparticles was examined at pH = 7 using fixed concentrations (50 mg L⁻¹) of different dyes solutions, namely basic fuchsine (BF), crystal violet (CV), malachite green (MG), and methyl orange (MO). After adsorption, the remaining dye concentration was obtained at a maximum wavelength of 545 for BF, 590 nm for CV, 579 nm for MG, and 465 nm for MO. Figure 8b presents the removal percentages of different dyes eliminated by MgO nanoparticles. Outcomes show that the elimination ability percentages of BF, CV, MG, and MO were 98%, 93%, 92%, and 30%, respectively. However, BF, CV, and MG dye uptakes were higher than MO dye uptake. The investigation of MgO nanorods with different dyes suggests the high adsorption selectivity towards cationic dyes (BF, CV, and MG) compared with MO dye.

4. Conclusions

The precipitation method was successfully employed to fabricate MgO nanorods. The obtained results displayed an excellent elimination efficiency toward BF dye. The impact of BF concentration and pH were scrutinized to improve the removal performance of the MgO nanorods. Batch experimental studies revealed that the BF dye removal onto MgO nanorods was pH-dependent with a maximum adsorption capacity at pH = 11 for BF pollutant, i.e., 493.90 mg/g. The removal of BF by MgO nanorods was examined using different kinetic and adsorption models, and the best fit was provided by the PSO kinetics and Freundlich adsorption isotherm model. The BF adsorption mechanism was connected to the electrostatic attractions and hydrogen bond, as indicated by pH and FTIR studies. The examination of MgO as a potential sorbent for other dyes (CV, MG, and MO) revealed the overall great potential and high selectivity of the MgO nanorods for cationic dye elimination in wastewaters.

Author Contributions: Conceptualization, B.Y.A., M.R.A.E. and M.A.B.A.; methodology, M.G.G., F.A.M.A. and A.M.A.; software, M.A.B.A. and S.R.; validation, M.A.B.A. and B.Y.A.; formal analysis, M.G.G., F.A.M.A. and B.Y.A.; investigation, M.G.G. and M.A.B.A.; resources, F.A.M.A. and A.M.A.; data curation, M.A.B.A. and F.A.M.A.; writing—original draft preparation, M.A.B.A., M.G.G. and F.A.M.A.; writing—review and editing, M.R.A.E., S.R. and M.A.B.A.; visualization, S.R. and M.A.B.A.; supervision, M.R.A.E.; project administration, F.A.M.A. and M.G.G.; funding acquisition, M.A.B.A., M.G.G. and B.Y.A. All authors have read and agreed to the published version of the manuscript.

Funding: This research was funded by Scientific Research at Imam Mohammad Ibn Saud Islamic University, grant number RG-21-09-75.

Institutional Review Board Statement: Not applicable.

Informed Consent Statement: Not applicable.

Data Availability Statement: The data presented in this study are available on request from the corresponding author.

Acknowledgments: Authors extend their appreciation to the Deanship of Scientific Research at Imam Mohammad Ibn Saud Islamic University for funding this work through Research Group no RG-21-09-75.

Conflicts of Interest: The authors declare no conflict of interest.

References

1. Soni, S.; Bajpai, P.; Mittal, J.; Arora, C. Utilisation of cobalt doped Iron based MOF for enhanced removal and recovery of methylene blue dye from waste water. *J. Mol. Liq.* **2020**, *314*, 113642. [[CrossRef](#)]
2. Yuan, H.; Chen, L.; Cao, Z.; Hong, F.F. Enhanced decolourization efficiency of textile dye Reactive Blue 19 in a horizontal rotating reactor using strips of BNC-immobilized laccase: Optimization of conditions and comparison of decolourization efficiency. *Biochem. Eng. J.* **2020**, *156*, 107501. [[CrossRef](#)]
3. Bayramoglu, G.; Altintas, B.; Arica, M.Y. Adsorption kinetics and thermodynamic parameters of cationic dyes from aqueous solutions by using a new strong cation-exchange resin. *Chem. Eng. J.* **2009**, *152*, 339–346. [[CrossRef](#)]
4. Hunger, K. *Industrial Dyes: Chemistry, Properties, Applications*; John Wiley & Sons: Hoboken, NJ, USA, 2007.
5. Ong, S.-T.; Tan, S.-Y.; Khoo, E.-C.; Lee, S.-L.; Ha, S.-T. Equilibrium studies for Basic blue 3 adsorption onto durian peel (*Durio zibethinus* Murray). *Desalin. Water Treat.* **2012**, *45*, 161–169. [[CrossRef](#)]
6. Lee, H.-J.; Ong, S.-T. Immobilization of rambutan (*Nephelium lappaceum*) peel as a sorbent for Basic Fuchsin removal. *Environ. Prot. Eng.* **2017**, *43*, 169–181. [[CrossRef](#)]
7. Zargar, B.; Parham, H.; Hatamie, A. Modified iron oxide nanoparticles as solid phase extractor for spectrophotometric determination and separation of basic fuchsin. *Talanta* **2009**, *77*, 1328–1331. [[CrossRef](#)]
8. Soneta, Y.; Midorikawa, T.; Miyamura, K. Anomalous distortion and stacking column formation of [Ni(dmit)2][−] induced by propeller-shaped dye cations, crystal violet and basic fuchsin. *Bull. Chem. Soc. Jpn.* **2006**, *79*, 1060–1062. [[CrossRef](#)]
9. De O Salomon, Y.L.; Georgin, J.; Dos Reis, G.S.; Claudio Lima, É.; Oliveira, M.L.S.; Franco, D.S.P.; Netto, M.S.; Allasia, D.; Luis Dotto, G. Utilization of Pacara Earpod tree (*Enterolobium contortisilquum*) and Ironwood (*Caesalpinia leiostachya*) seeds as low-cost biosorbents for removal of basic fuchsin. *Environ. Sci. Pollut. Res.* **2020**, *27*, 33307–33320. [[CrossRef](#)]
10. Pathrose, B.; Nampoori, V.; Radhakrishnan, P.; Mujeeb, A. Investigations on the third order nonlinear optical properties of Basic Fuchsin dye using zscan technique. *Optik* **2016**, *127*, 7717–7725. [[CrossRef](#)]
11. Huang, L.; Kong, J.; Wang, W.; Zhang, C.; Niu, S.; Gao, B. Study on Fe(III) and Mn(II) modified activated carbons derived from *Zizania latifolia* to removal basic fuchsin. *Desalination* **2012**, *286*, 268–276. [[CrossRef](#)]
12. Yang, X.; Li, Y.; Du, Q.; Sun, J.; Chen, L.; Hu, S.; Wang, Z.; Xia, Y.; Xia, L. Highly effective removal of basic fuchsin from aqueous solutions by anionic polyacrylamide/graphene oxide aerogels. *J. Colloid Interface Sci.* **2015**, *453*, 107–114. [[CrossRef](#)] [[PubMed](#)]
13. Rath, B.S.; Kumar, P.S. Sustainable approach on the biodegradation of azo dyes: A short review. *Curr. Opin. Green Sustain. Chem.* **2022**, *33*, 100578. [[CrossRef](#)]
14. Bianchi, C.L.; Djellabi, R.; Della Pina, C.; Falletta, E. Doped-polyaniline based sorbents for the simultaneous removal of heavy metals and dyes from water: Unravelling the role of synthesis method and doping agent. *Chemosphere* **2022**, *286*, 131941. [[CrossRef](#)] [[PubMed](#)]
15. Kumar, A.; Rana, A.; Sharma, G.; Naushad, M.; Dhiman, P.; Kumari, A.; Stadler, F.J. Recent advances in nano-Fenton catalytic degradation of emerging pharmaceutical contaminants. *J. Mol. Liq.* **2019**, *290*, 111177. [[CrossRef](#)]
16. Su, M.; Li, H.; He, X.; Xu, Z. Significant enhancement of pesticide and organic dyes degradation by ion-exchange within a metal-organic framework. *Polyhedron* **2022**, *215*, 115651. [[CrossRef](#)]
17. Aziz, H.A.; Tajarudin, H.A.; Wei, T.H.L.; Alazaiza, M.Y.D. Iron and manganese removal from groundwater using limestone filter with iron-oxidized bacteria. *Int. J. Environ. Sci. Technol.* **2020**, *17*, 2667–2680. [[CrossRef](#)]

18. Ben Aissa, M.A.; Khezami, L.; Taha, K.; Elamin, N.; Mustafa, B.; Al-Ayed, A.S.; Modwi, A. Yttrium oxide-doped ZnO for effective adsorption of basic fuchsin dye: Equilibrium, kinetics, and mechanism studies. *Int. J. Environ. Sci. Technol.* **2021**, *1*–14. [[CrossRef](#)]
19. Diawara, M.; Kamissoko, M.; Rahali, S.; Samaké, D.; Tamboura, M.; Diawara, B.; Seydou, M. A Computational Exploration of Ammonia Adsorption on the Kaolinite Clay Surface. *Chem. Afr.* **2021**, *4*, 905–914. [[CrossRef](#)]
20. Abdulkhair, B.; Salih, M.; Modwi, A.; Adam, F.; Elamin, N.; Seydou, M.; Rahali, S. Adsorption behavior of barium ions onto ZnO surfaces: Experiments associated with DFT calculations. *J. Mol. Struct.* **2021**, *1223*, 128991. [[CrossRef](#)]
21. Sharma, G.; Kumar, A.; Naushad, M.; Thakur, B.; Vo, D.-V.N.; Gao, B.; Al-Kahtani, A.A.; Stadler, F.J. Adsorptive-photocatalytic removal of fast sulphon black dye by using chitin-cl-poly (itaconic ac-id-co-acrylamide)/zirconium tungstate nanocomposite hydrogel. *J. Hazardous Mater.* **2021**, *416*, 125714. [[CrossRef](#)]
22. Pishnamazi, M.; Khan, A.; Kurniawan, T.A.; Sanaeepur, H.; Albadarin, A.B.; Soltani, R. Adsorption of dyes on multifunctionalized nano-silica KCC-1. *J. Mol. Liq.* **2021**, *338*, 116573. [[CrossRef](#)]
23. Rahali, S.; Ali Ben Aissa, M.; Khezami, L.; Elamin, N.; Seydou, M.; Moidwi, A. Adsorption Behavior of Congo Red onto Barium-Doped ZnO Nanoparticles: Correlation between Experimental Results and DFT Calculations. *Langmuir* **2021**, *37*, 7285–7294. [[CrossRef](#)]
24. Modwi, A.; Khezami, L.; Ghoniem, M.G.; Nguyen-Tri, P.; Baaloudj, O.; Guesmi, A.; AlGethami, F.K.; Amer, M.S.; Assadi, A.A. Superior removal of dyes by mesoporous MgO/g-C₃N₄ fabricated through ultrasound method: Adsorption mechanism and process modeling. *Environ. Res.* **2022**, *205*, 112543. [[CrossRef](#)] [[PubMed](#)]
25. Qin, P.; Yang, Y.; Zhang, X.; Niu, J.; Yang, H.; Tian, S.; Zhu, J.; Lu, M. Highly Efficient, Rapid, and Simultaneous Removal of Cationic Dyes from Aqueous Solution Using Monodispersed Mesoporous Silica Nanoparticles as the Adsorbent. *Nanomaterials* **2018**, *8*, 4. [[CrossRef](#)] [[PubMed](#)]
26. Sharifpour, E.; Ghaedi, M.; Asfaram, A.; Farsadrooh, M.; Dil, E.A.; Javadian, H. Modeling and optimization of ultrasound-assisted high performance adsorption of Basic Fuchsin by starch-capped zinc selenide nanoparticles/AC as a novel composite using response surface methodology. *Int. J. Biol. Macromol.* **2020**, *152*, 913–921. [[CrossRef](#)] [[PubMed](#)]
27. Modwi, A.; Khezami, L.; Taha, K.K.; Idriss, H. Flower Buds Like MgO Nanoparticles: From Characterisation to Indigo Carmine Elimination. *Z. Naturforschung A* **2018**, *73*, 975–983. [[CrossRef](#)]
28. Sharma, A.; Arya, S.; Singh, B.; Prerna; Tomar, A.; Singh, S.; Sharma, R. Sol-Gel Synthesis of Zn Doped MgO Nanoparticles and Their Applications. *Integr. Ferroelectr.* **2020**, *205*, 14–25. [[CrossRef](#)]
29. Meng, A.; Xing, J.; Li, Z.; Li, Q. Cr-Doped ZnO Nanoparticles: Synthesis, Characterization, Adsorption Property, and Recyclability. *ACS Appl. Mater. Interfaces* **2015**, *7*, 27449–27457. [[CrossRef](#)]
30. Xiong, C.; Wang, W.; Tan, F.; Luo, F.; Chen, J.; Qiao, X. Investigation on the efficiency and mechanism of Cd(II) and Pb(II) removal from aqueous solutions using MgO nanoparticles. *J. Hazard. Mater.* **2015**, *299*, 664–674. [[CrossRef](#)]
31. Wu, P.-Y.; Jiang, Y.-P.; Zhang, Q.-Y.; Jia, Y.; Peng, D.-Y.; Xu, W. Comparative study on arsenate removal mechanism of MgO and MgO/TiO₂ composites: FTIR and XPS analysis. *N. J. Chem.* **2016**, *40*, 2878–2885. [[CrossRef](#)]
32. Xu, S.; Zhong, Z.; Liu, W.; Deng, H.; Lin, Z. Removal of Sb(III) from wastewater by magnesium oxide and the related mechanisms. *Environ. Res.* **2020**, *186*, 109489. [[CrossRef](#)] [[PubMed](#)]
33. Liu, Y.; Li, Q.; Gao, S.; Shang, J.K. Exceptional As(III) Sorption Capacity by Highly Porous Magnesium Oxide Nanoflakes Made from Hydrothermal Synthesis. *J. Am. Ceram. Soc.* **2011**, *94*, 217–223. [[CrossRef](#)]
34. Condon, J.B. *Surface Area and Porosity Determinations by Physisorption: Measurements and Theory*; Elsevier: Amsterdam, The Netherlands, 2006.
35. Elkady, M.; Ibrahim, A.; El-Latif, M.A. Assessment of the adsorption kinetics, equilibrium and thermodynamic for the potential removal of reactive red dye using eggshell biocomposite beads. *Desalination* **2011**, *278*, 412–423. [[CrossRef](#)]
36. Bessashia, W.; Berredjem, Y.; Hattab, Z.; Bououdina, M. Removal of Basic Fuchsin from water by using mussel powdered eggshell membrane as novel bioadsorbent: Equilibrium, kinetics, and thermodynamic studies. *Environ. Res.* **2020**, *186*, 109484. [[CrossRef](#)]
37. Sharma, G.; Kumar, A.; Chauhan, C.; Okram, A.; Sharma, S.; Pathania, D.; Kalia, S. Pectin-crosslinked-guar gum/SPION nanocomposite hydrogel for adsorption of m-cresol and o-chlorophenol. *Sustain. Chem. Pharm.* **2017**, *6*, 96–106.
38. Brito, S.M.D.O.; Andrade, H.M.C.; Soares, L.F.; de Azevedo, R.P. Brazil nut shells as a new biosorbent to remove methylene blue and indigo carmine from aqueous solutions. *J. Hazard. Mater.* **2010**, *174*, 84–92. [[CrossRef](#)]
39. Futamata, M.; Yu, Y.; Yajima, T. Elucidation of electrostatic interaction between cationic dyes and Ag nanoparticles generating enormous SERS enhancement in aqueous solution. *J. Phys. Chem. C* **2011**, *115*, 5271–5279. [[CrossRef](#)]
40. Moawed, E.A.; Alqarni, Y. Determination of azine and triphenyl methane dye in wastewater using polyurethane foam functionalized with tannic acid. *Sample Prep.* **2013**, *1*, 18–27. [[CrossRef](#)]
41. Zhang, J.-Z. Avoiding spurious correlation in analysis of chemical kinetic data. *Chem. Commun.* **2011**, *47*, 6861–6863. [[CrossRef](#)]
42. Elamin, M.R.; Abdulkhair, B.Y.; Algethami, F.K.; Khezami, L. Linear and nonlinear investigations for the adsorption of paracetamol and metformin from water on acid-treated clay. *Sci. Rep.* **2021**, *11*, 1–13. [[CrossRef](#)]
43. Acharya, J.; Sahu, J.N.; Mohanty, C.; Meikap, B. Removal of lead(II) from wastewater by activated carbon developed from Tamarind wood by zinc chloride activation. *Chem. Eng. J.* **2009**, *149*, 249–262. [[CrossRef](#)]
44. Mallakpour, S.; Tabesh, F. Tragacanth gum based hydrogel nanocomposites for the adsorption of methylene blue: Comparison of linear and non-linear forms of different adsorption isotherm and kinetics models. *Int. J. Biol. Macromol.* **2019**, *133*, 754–766. [[CrossRef](#)] [[PubMed](#)]

45. El-Khaiary, M.I.; Malash, G.F.; Ho, Y.-S. On the use of linearized pseudo-second-order kinetic equations for modeling adsorption systems. *Desalination* **2010**, *257*, 93–101. [[CrossRef](#)]
46. Naghizadeh, A.; Karimi, A.; Derakhshani, E.; Esform, A. Single-walled carbon nanotubes (SWCNTs) as an efficient adsorbent for removal of reactive dyes from water solution: Equilibrium, kinetic, and thermodynamic. *Environ. Qual. Manag.* **2021**, 1–8. [[CrossRef](#)]
47. Debnath, S.; Ghosh, U.C. Equilibrium modeling of single and binary adsorption of Cd (II) and Cu (II) onto agglom-erated nano structured titanium (IV) oxide. *Desalination* **2011**, *273*, 330–342. [[CrossRef](#)]
48. Boyd, G.E.; Adamson, A.W.; Myers, L.S. The Exchange Adsorption of Ions from Aqueous Solutions by Organic Zeolites. II. Kinetics1. *J. Am. Chem. Soc.* **1947**, *69*, 2836–2848. [[CrossRef](#)]
49. Chien, S.H.; Clayton, W.R. Application of Elovich Equation to the Kinetics of Phosphate Release and Sorption in Soils. *Soil Sci. Soc. Am. J.* **1980**, *44*, 265–268. [[CrossRef](#)]
50. Alrobei, H.; Prashanth, M.; Manjunatha, C.; Kumar, C.P.; Chitrabanu, C.; Shivaramu, P.D.; Kumar, K.Y.; Raghu, M. Adsorption of anionic dye on eco-friendly synthesised reduced graphene oxide anchored with lanthanum aluminate: Isotherms, kinetics and statistical error analysis. *Ceram. Int.* **2021**, *47*, 10322–10331. [[CrossRef](#)]
51. Li, M.; Lan, P.; Liao, Y.; Sun, S.; Liu, H. Novel CaCO₃/chitin aerogel: Synthesis and adsorption performance toward Congo red in aqueous solutions. *Int. J. Biol. Macromol.* **2021**, *181*, 786–792.
52. Al-Ghouti, M.A.; Razavi, M.M. Water Reuse: Brackish water desalination using *Prosopis juliflora*. *Environ. Technol. Innov.* **2020**, *17*, 100614. [[CrossRef](#)]
53. Ayawei, N.; Ebelegi, A.N.; Wankasi, D. Modelling and Interpretation of Adsorption Isotherms. *J. Chem.* **2017**, *2017*, 3039817. [[CrossRef](#)]
54. Al-Ghouti, M.A.; Da'Ana, D.A. Guidelines for the use and interpretation of adsorption isotherm models: A review. *J. Hazard. Mater.* **2020**, *393*, 122383. [[CrossRef](#)] [[PubMed](#)]
55. Günay, A.; Arslankaya, E.; Tosun, I. Lead removal from aqueous solution by natural and pretreated clinoptilolite: Ad-sorption equilibrium and kinetics. *J. Hazard. Mater.* **2007**, *146*, 362–371. [[CrossRef](#)] [[PubMed](#)]
56. Treybal, R.E. *Mass Transfer Operations*; McGraw-Hill Book Company: New York, NY, USA, 1980; p. 466.
57. Demiral, H.; Demiral, I.; Tümsük, F.; Karabacakoglu, B. Adsorption of chromium(VI) from aqueous solution by activated carbon derived from olive bagasse and applicability of different adsorption models. *Chem. Eng. J.* **2008**, *144*, 188–196. [[CrossRef](#)]
58. Mondal, N.K.; Basu, S. Potentiality of waste human hair towards removal of chromium(VI) from solution: Kinetic and equilibrium studies. *Appl. Water Sci.* **2019**, *9*, 49. [[CrossRef](#)]
59. Zhang, H.; Hu, J.; Xie, J.; Wang, S.; Cao, Y. A solid-state chemical method for synthesizing MgO nanoparticles with superior adsorption properties. *RSC Adv.* **2019**, *9*, 2011–2017. [[CrossRef](#)]
60. Khan, T.A.; Khan, E.A.; Shahjahan. Removal of basic dyes from aqueous solution by adsorption onto binary iron-manganese oxide coated kaolinite: Non-linear isotherm and kinetics modeling. *Appl. Clay Sci.* **2015**, *107*, 70–77. [[CrossRef](#)]
61. Mohammed, B.B.; Hsini, A.; Abdellaoui, Y.; Oualid, H.A.; Laabd, M.; El Ouardi, M.; Addi, A.A.; Yamni, K.; Tijani, N. Fe-ZSM-5 zeolite for efficient removal of basic Fuchsin dye from aqueous solutions: Synthesis, characterization and adsorption process optimization using BBD-RSM modeling. *J. Environ. Chem. Eng.* **2020**, *8*, 104419. [[CrossRef](#)]
62. Guan, Y.; Wang, S.; Wang, X.; Sun, C.; Wang, Y.; Hu, L. Preparation of mesoporous Al-MCM-41 from natural palygorskite and its adsorption performance for haz-ardous aniline dye-basic fuchsin. *Microporous Mesoporous Mater.* **2018**, *265*, 266–274. [[CrossRef](#)]
63. Hinojosa-Reyes, M.; Camposeco-Solis, R.; Ruiz, F. H₂Ti₃O₇ titanate nanotubes for highly effective adsorption of basic fuchsin dye for water purification. *Microporous Mesoporous Mater.* **2018**, *276*, 183–191. [[CrossRef](#)]
64. Lu, T.; Wang, L.; He, Y.; Chen, J.; Wang, R.-M. Loess surface grafted functional copolymer for removing basic fuchsin. *RSC Adv.* **2017**, *7*, 18379–18383. [[CrossRef](#)]
65. Singha, N.R.; Karmakar, M.; Mahapatra, M.; Mondal, H.; Dutta, A.; Roy, C.; Chattopadhyay, P.K. Systematic synthesis of pectin-g-(sodium acrylate-co-N-isopropylacrylamide) interpenetrating polymer network for superadsorption of dyes/M(ii): Determination of physicochemical changes in loaded hydrogels. *Polym. Chem.* **2017**, *8*, 3211–3237. [[CrossRef](#)]